Mimicking the Veselago-Pendry lens with broadband matched double-negative metamaterials

João T. Costa and Mário G. Silveirinha[*]

University of Coimbra, Department of Electrical Engineering, Instituto de Telecomunicações, Coimbra, Portugal
(Received 27 June 2011; revised manuscript received 21 September 2011; published 19 October 2011)

Most metamaterial designs are based on the resonant response of either high permittivity or metallic particles embedded in a dielectric host (e.g. an array of metallic particles standing in air). As a consequence, the response of the material is typically narrowband, and this holds back many interesting applications. Here, we show that the key to achieve a broadband isotropic response may lie on a low-permittivity host with a plasmonic-type response. In particular, we demonstrate that a host medium with such characteristics may enable an effective permittivity ε_{eff} and permeability μ_{eff} simultaneously negative in a frequency range that may be quite broad as compared to typical designs based on metallic particles standing in a dielectric host. It is shown that the proposed configuration is largely insensitive to disorder and that a slab of the metamaterial may mimic to some extent the Veselago–Pendry's superlens, enabling negative refraction and imaging with super-resolution.

I. INTRODUCTION

In 1968, Veselago[1] theoretically investigated the electromagnetic behavior of a medium having both electric permittivity ε and magnetic permeability μ negative (DNG material) and concluded that such a medium would have propagation properties radically different from right-handed materials with both ε and μ greater than zero. About 10 years ago, building on Veselago's work, Pendry suggested that a lossless material slab with negative index of refraction ($n = -1$ at a fixed frequency of operation) makes a perfect lens with resolution independent of the wavelength of operation and of the polarization of the light.[2] Such an extraordinary phenomenon has its roots in two effects: on one hand, the propagating plane waves are focused due to negative refraction; on the other hand, the evanescent modes are restored due to resonant excitation of guided modes supported by the double-negative medium when $\varepsilon = \mu = -1$. Nevertheless, it soon became evident that this imaging mechanism is strongly sensitive to losses and material dispersion,[3–5] besides the numerous practical difficulties related to the realization of double-negative media. A promising route to realize metamaterials with simultaneously negative ε and μ is based on periodic arrays of plasmonic particles.[6–9] It is well known that nanoparticles with negative permittivity can support multiple electric resonances,[10] and such resonances can indeed be useful if one wishes to tailor the effective properties of a composite material (particularly the magnetic response in the optical regime). However, such inherently electrostatic resonances may also be a source of sharp singularities in the effective response ε_{eff} of a composite material and, in practice, may imply strong spatial dispersion and imply that the frequency range where the response of the effective medium is useful be quite narrow. For example, in Ref. 6, it was shown that a periodic array of plasmonic cylindrical inclusions supports many high-multipole resonances when the real part of the permittivity of the inclusion satisfies $\varepsilon'(\omega) \approx -1$ and that some of these resonances may be associated with a regime where the structure behaves as a DNG material. However, the frequency window where the effective permittivity ε_{eff} and effective permeability μ_{eff} are simultaneously negative is very narrow due to the sensitive behavior of ε_{eff} in the DNG

regime. In other words, when the inclusions are operated near the plasmonic resonance, the characteristic wavelength of a guided mode may be shorter than the lattice constant, and in such a case, the material cannot be regarded as an effective medium, and thus it cannot be homogenized.

The main goal of this paper is to demonstrate that by interchanging the roles of the dielectric host material and of the plasmonic inclusions, it may be possible to circumvent the above mentioned drawbacks and achieve a broadband DNG regime, where the response of the effective medium is to a good approximation local (effects of spatial dispersion are weak) and largely insensitive both to disorder and in part to loss effects. Moreover, we show that in the case of sufficiently low loss, such a configuration may enable mimicking to some extent the Veselago–Pendry's lens and imaging with super-resolution. In this work, a time-harmonic variation $e^{-i\omega t}$ is considered.

II. LIMITATIONS OF DNG METAMATERIALS BASED ON PLASMONIC-TYPE INCLUSIONS

In order to further illustrate the inherent bandwidth limitations of designs based on plasmonic-type inclusions, next we characterize the effective parameters (ε_{eff} and μ_{eff}) of a configuration formed by an array of plasmonic inclusions arranged in a square lattice with lattice constant a [inset of Fig. 2(b)]. The inclusions are cylinders with a circular cross-section with radius R. The dielectric permittivity ε_r of the inclusions is described by the Drude model $\varepsilon_r = 1 - \frac{\omega_p^2}{\omega(\omega + i\Gamma)}$ where ω_p is the plasma frequency and Γ is the collision frequency. The Drude dispersion model may describe accurately the response of noble metals through the infrared and optical domains. The host region is a vacuum. It is assumed that the cylinders have a normalized radius $R/a = 0.44$, the plasma frequency is such that $\omega_p a/c = 1.0$ and the collision frequency is $\Gamma/\omega_p = 0.001$. To characterize the effective response, we assume that the metamaterial can be accurately described by an effective permittivity $\varepsilon_{\text{eff}} = \varepsilon(\omega)$ and an effective permeability $\mu_{\text{eff}} = \mu(\omega)$ (for simplicity, here we restrict our discussion to the case of isotropic media and assume there is no magneto-electric coupling). The electric field is assumed
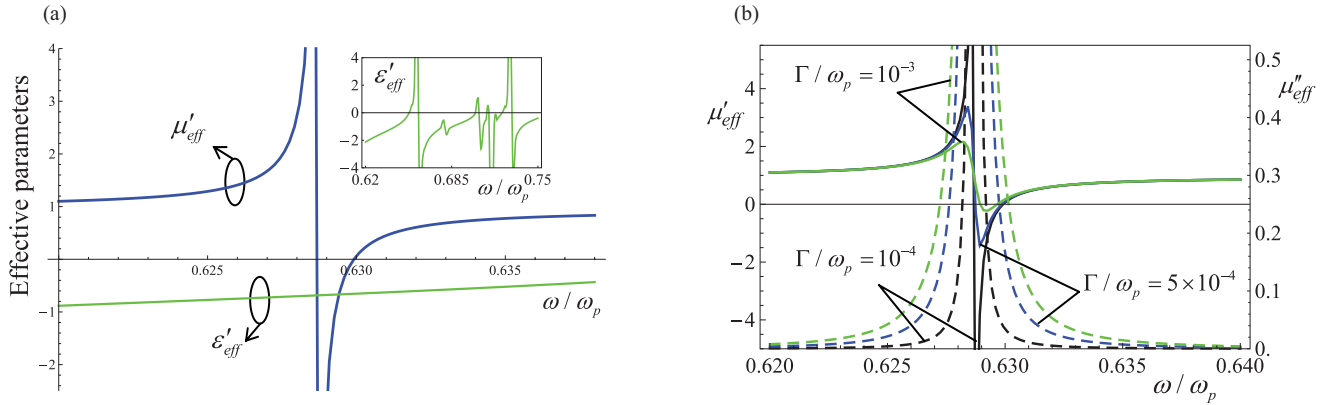
(a)

(b)

FIG. 1. (Color online) (a) Real parts of the effective permittivity $\varepsilon_{\mathrm{eff}} = \varepsilon'_{\mathrm{eff}} + i\varepsilon''_{\mathrm{eff}}$ (green curves) and permeability $\mu_{\mathrm{eff}} = \mu'_{\mathrm{eff}} + i\mu''_{\mathrm{eff}}$ (blue curves) as a function of the normalized frequency ω/ω_p ($\Gamma/\omega_p = 10^{-4}$). The inset shows the real part of the effective permittivity ($\Gamma/\omega_p = 10^{-4}$) in the vicinity of the plasmonic resonance of the inclusions ($\omega/\omega_p = 0.7$). (b) Real and imaginary parts of the effective permeability $\mu_{\mathrm{eff}} = \mu'_{\mathrm{eff}} + i\mu''_{\mathrm{eff}}$ as a function of the normalized frequency ω/ω_p, for different values of the damping frequency: $\Gamma/\omega_p = 10^{-4}$ (black curves), $\Gamma/\omega_p = 5 \times 10^{-4}$ (blue curves) and $\Gamma/\omega_p = 10^{-3}$ (green curves). The solid lines correspond to the real part of μ_{eff}, while the dashed lines represent the imaginary part.

to lie in the *xoy* plane, whereas the magnetic field is directed along the *z* direction. We characterize the effective response of the metamaterial in a two-step process: First, the nonlocal (spatially dispersive) dielectric function of the metamaterial $\overline{\overline{\varepsilon}}_{\mathrm{eff}}(\omega, \mathbf{k})$ is numerically computed, as described in Refs. 11 and 12. Then, in a second step, the local parameters are extracted from the nonlocal dielectric function using: $\varepsilon(\omega) = \varepsilon_{\mathrm{eff}}(\omega, \mathbf{k} = 0)/\varepsilon_0$ and $\mu(\omega) = 1 + (1 - \frac{1}{2\varepsilon_0}\frac{\omega^2}{c^2}\frac{\partial^2 \varepsilon_{\mathrm{eff},yy}}{\partial k_x^2}|_{\mathbf{k}=0})^{-1}$. For more details, see Ref. 11. The calculated effective parameters are depicted as a function of the frequency in Fig. 1(b), confirming that the frequency window where both $\varepsilon_{\mathrm{eff}}$ and μ_{eff} are simultaneously negative is extremely narrow ($0.629 < \omega/\omega_p < 0.630$, i.e. the bandwidth is less than 0.2%). Our computed results are qualitatively analogous to those reported in Ref. 6 for a similar geometrical structure. The inset of Fig. 1(a) illustrates the irregular behavior of the effective permittivity $\varepsilon_{\mathrm{eff}}$ in the vicinity of $\omega = 0.7\omega_p$ (where $\varepsilon'_r \approx -1$), caused by the excitation of multiple quasistatic resonances. In order to determine how the effective response of this configuration is affected by losses, in Fig. 1(b), we depict the effective permeability $\mu_{\mathrm{eff}} = \mu'_{\mathrm{eff}} + i\mu''_{\mathrm{eff}}$ at the resonance for different values of absorption, i.e. for different values of Γ. It is clear from Fig. 1(b) that even for extremely low values of absorption ($\Gamma/\omega_p = 5 \times 10^{-4}$, blue curves) the magnetic resonance is tremendously damped, and it almost disappears when a slightly higher value of loss is considered ($\Gamma/\omega_p = 1 \times 10^{-3}$, green curves), confirming that the DNG response of this configuration is not only extremely narrowband but also very sensitive to the effect of loss.

III. BROADBAND MATCHED DNG METAMATERIALS

The example of the previous section illustrates the inherent bandwidth restrictions and high loss sensitivity of typical metamaterial designs based on materials with a plasmonic-type response. Surprisingly, as described next, there may be a simple strategy to overcome these apparently fundamental limitations and achieve a broadband low loss response.

Notably, this may involve simply interchanging the roles of the inclusions and of the host material. The idea of considering a metamaterial with a design based on its complementary structure was also considered in Ref. 13 in a different context.

In order that DNG materials can be used effectively as functional elements of novel electromagnetic devices it is essential that they can be efficiently coupled to conventional dielectrics. In practice, this requires that the impedance of the DNG material, η, is relatively close to the impedance of vacuum $\eta_0 = \sqrt{\mu_0/\varepsilon_0}$, or equivalently that $\mu \sim \varepsilon$, being ε and μ the relative permittivity and permeability of the DNG material, respectively. Hence, in an ideal scenario, we would like to have matched operation, $\mu = \varepsilon$, over a broad frequency region.

An interesting possibility of having matched operation in the regime where the effective parameters are simultaneously near zero [$\varepsilon_{\mathrm{eff}}(\omega_p) \approx \mu_{\mathrm{eff}}(\omega_p) \approx 0$] was described in Ref. 14, and involves embedding dielectric particles with suitable size and permittivity in a host background with near-zero permittivity.[15] The analysis of Ref. 14, was however focused in the regime $\varepsilon_{\mathrm{eff}} \approx \mu_{\mathrm{eff}} \approx 0$ (for geometries that are intrinsically two dimensional), and the possibility of having matched operation over a broad frequency band or superlensing ($\varepsilon_{\mathrm{eff}} \approx \mu_{\mathrm{eff}} \approx -1$) was not investigated. However, it is evident that causality and passivity restrictions imply that for small absorption both $\varepsilon_{\mathrm{eff}}(\omega)$ and $\mu_{\mathrm{eff}}(\omega)$ must increase with frequency,[16] and hence if $\varepsilon_{\mathrm{eff}} \approx \mu_{\mathrm{eff}} \approx 0$ at a given frequency ω_p, then for $\omega < \omega_p$ the effective permittivity and permeability are simultaneously negative. Next, we build on these ideas and demonstrate that a metamaterial formed by dielectric inclusions embedded in a plasmonic host enables, indeed, a broadband DNG regime, even in fully three-dimensional scenarios.

The first configuration that we will analyze is related to that in Sec. II, i.e. an array of cylinders arranged in a square lattice with lattice constant a; however, now we suppose that the cylinders have a high-index permittivity ε_r and that the permittivity of the host material ε_h is described by the Drude dispersion model (see the inset of Fig. 2). It is assumed that
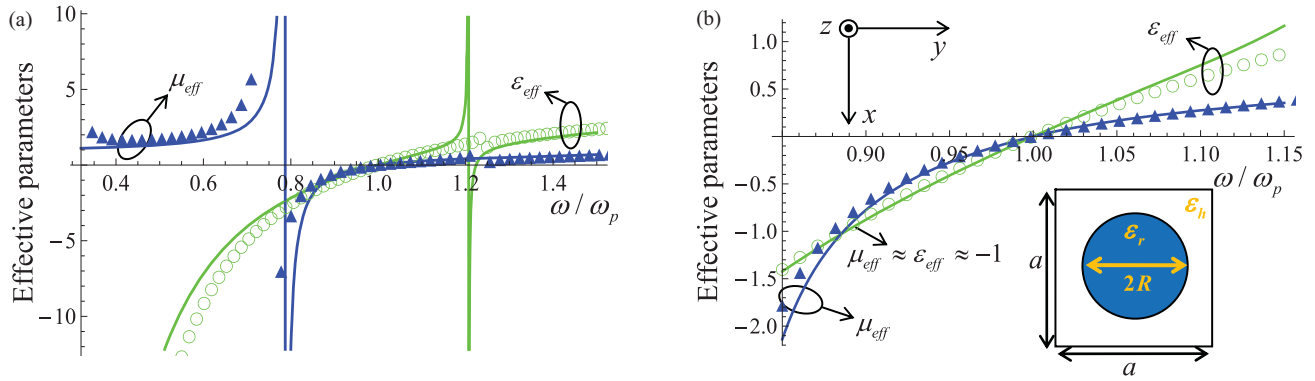
FIG. 2. (Color online) (a) Effective permittivity ε_{eff} (green curves) and permeability μ_{eff} (blue curves) ($\Gamma/\omega_p = 0$) as a function of the normalized frequency ω/ω_p. The discrete symbols were calculated using full wave homogenization (Ref. 11), and the solid lines are obtained using the Clausius−Mossotti formula. (b) Same as (a) but the effective parameters are depicted in a narrower frequency band. The geometry of the unit cell is shown in the inset: it consists of a cylindrical inclusion with circular cross-section with normalized radius R/a and permittivity ε_r embedded in a host medium with permittivity ε_h described by a Drude-type dispersion model.

the plasma frequency is such that $\omega_p a/c = 1.0$, and first, we will consider the case wherein the material is lossless, i.e. $\Gamma/\omega_p = 0$. Using the theory of Ref. 14, we have chosen the normalized radius of the cylinders ($R/a = 0.435$) and the dielectric permittivity $\varepsilon_r \approx 50.47$ in such a way that at $\omega = \omega_p$ the structure behaves as a zero-index material with simultaneously near-zero permittivity and permeability and, consequently, as a left-handed material for $\omega < \omega_p$.

The effective parameters $\varepsilon_{\text{eff}}(\omega)$ and $\mu_{\text{eff}}(\omega)$ calculated using the full-wave homogenization[11] are depicted as a function of frequency in Fig. 2(a) (discrete symbols); the same parameters are shown in Fig. 2(b) but over a narrower spectral region. As in Sec. II, the electric field is assumed to lie in the xoy plane, whereas the magnetic field is directed along the z direction. Consistent with the theory of Ref. 14, both the permittivity and permeability are near zero at the plasma frequency $\varepsilon_{\text{eff}}(\omega_p) = \mu_{\text{eff}}(\omega_p) \approx 0$. It is also seen that $\varepsilon_{\text{eff}}(\omega)$ and $\mu_{\text{eff}}(\omega)$ are simultaneously positive for $1.0 < \omega/\omega_p < 1.2$, and simultaneously negative for $0.8 < \omega/\omega_p < 1.0$, being the bandwidth of the DNG regime several orders of magnitude wider than what is achievable when the roles of the inclusions and host are interchanged, as discussed in Sec. II (e.g. in one of the examples of Sec. II, the DNG bandwidth was less than 0.2%). The solid curves of Fig. 2 represent the effective parameters calculated using the Clausius–Mossotti (CM) mixing formulas,[17] and concur rather well with the results obtained with our numerical homogenization formalism. The effective permittivity $\varepsilon_{\text{eff}}(\omega)$ and the effective magnetic permeability $\mu_{\text{eff}}(\omega)$ were calculated using Eqs. (20) and (23) of Ref. 14, respectively. In Fig. 2, it is also possible to observe that the effective parameters calculated using the full-wave homogenization[11] are such that $\varepsilon_{\text{eff}}(\omega) \approx \mu_{\text{eff}}(\omega) \approx -1$ at $\omega a/c = 0.88$. In fact, using the CM formulas, it is possible to fine tune the geometry in such a way that $\varepsilon_{\text{eff}}(\omega) \approx \mu_{\text{eff}}(\omega)$ in the DNG regime, ensuring a good matching with free space in a wide frequency window. Notably, at $\omega a/c = 0.88$, the response of a planar metamaterial slab may mimic to some extent the Veselago–Pendry's lens,[1,2] as we will discuss ahead.

Next, we analyze the robustness with respect to loss of the proposed configuration by calculating the effective parameters

$\varepsilon_{\text{eff}}(\omega)$ and $\mu_{\text{eff}}(\omega)$ when losses are taken into account (Fig. 3; these results were computed using the full-wave homogenization method).[11] In Fig. 3(a), it can be seen that when the damping frequency of the host is increased to $\Gamma/\omega_p = 0.01$, the effective permittivity $\varepsilon_{\text{eff}} = \varepsilon'_{\text{eff}} + i\varepsilon''_{\text{eff}}$ (green curves) and permeability $\mu_{\text{eff}} = \mu'_{\text{eff}} + i\mu''_{\text{eff}}$ (blue curves) are barely affected, i.e. our material remains tuned so that $\varepsilon'_{\text{eff}}(\omega) \approx \mu'_{\text{eff}}(\omega) \approx -1$ at $\omega a/c = 0.88$ and $\varepsilon'_{\text{eff}}(\omega_p) = \mu'_{\text{eff}}(\omega_p) \approx 0$. This contrasts sharply with the response of the complementary structure described in Sec. II, which is strongly affected by loss, and indicates that the present configuration is far more robust in this regard. Interestingly, the loss in the host medium affects mainly the imaginary part of ε_{eff} (green dashed curve) given that $\mu''_{\text{eff}}(\omega) \approx 0$, whereas $0.023 < \varepsilon''_{\text{eff}}(\omega) < 1.0$. Notably, these general conclusions still hold when the loss of the host medium is increased by one order of magnitude [$\Gamma/\omega_p = 0.1$, Fig. 3(b)]. Indeed, consistent with the results of Fig. 3(a), when $\Gamma/\omega_p = 0.1$ the imaginary part of the effective magnetic permeability remains negligible.

Figure 3(c) reports the effect of loss in the cylindrical dielectric inclusion ($\varepsilon_r = \varepsilon'_r + i\varepsilon''_r$) when the loss tangent of the dielectric is $\varepsilon''_r/\varepsilon'_r = 0.1$. In this case, the effective magnetic response is more affected by loss, and in particular, the magnetic permeability is detuned so that $\mu'_{\text{eff}}(\omega) \neq -1$ at $\omega a/c = 0.88$. Nevertheless, even though the effective magnetic permeability μ_{eff} is shifted when lossy inclusions are considered, the effective response of the material remains broadband. Curiously, different from Figs. 3(a) and 3(b), wherein for a lossy host the imaginary part of the magnetic permeability $\mu''_{\text{eff}}(\omega)$ was almost zero valued, for lossy dielectric inclusions, we notice the opposite behavior, i.e. $\varepsilon''_{\text{eff}}(\omega) \approx 0$. Finally, Fig. 3(d) reports the combined effect of loss in the plasmonic host and loss in the dielectric inclusions, and it is seen that the two mechanisms of loss add up, resulting in moderate loss in both the effective permittivity and permeability.

In Fig. 4(a), we depict the dispersion diagram obtained by solving $k^2 = \frac{\omega^2}{c^2}\varepsilon_{\text{eff}}\mu_{\text{eff}}$ around the plasma frequency, for the case $\Gamma/\omega_p = 0$. The blue circles were obtained using our homogenization method,[11] whereas the green diamonds were calculated using the Clausius–Mossotti theory.[14] The
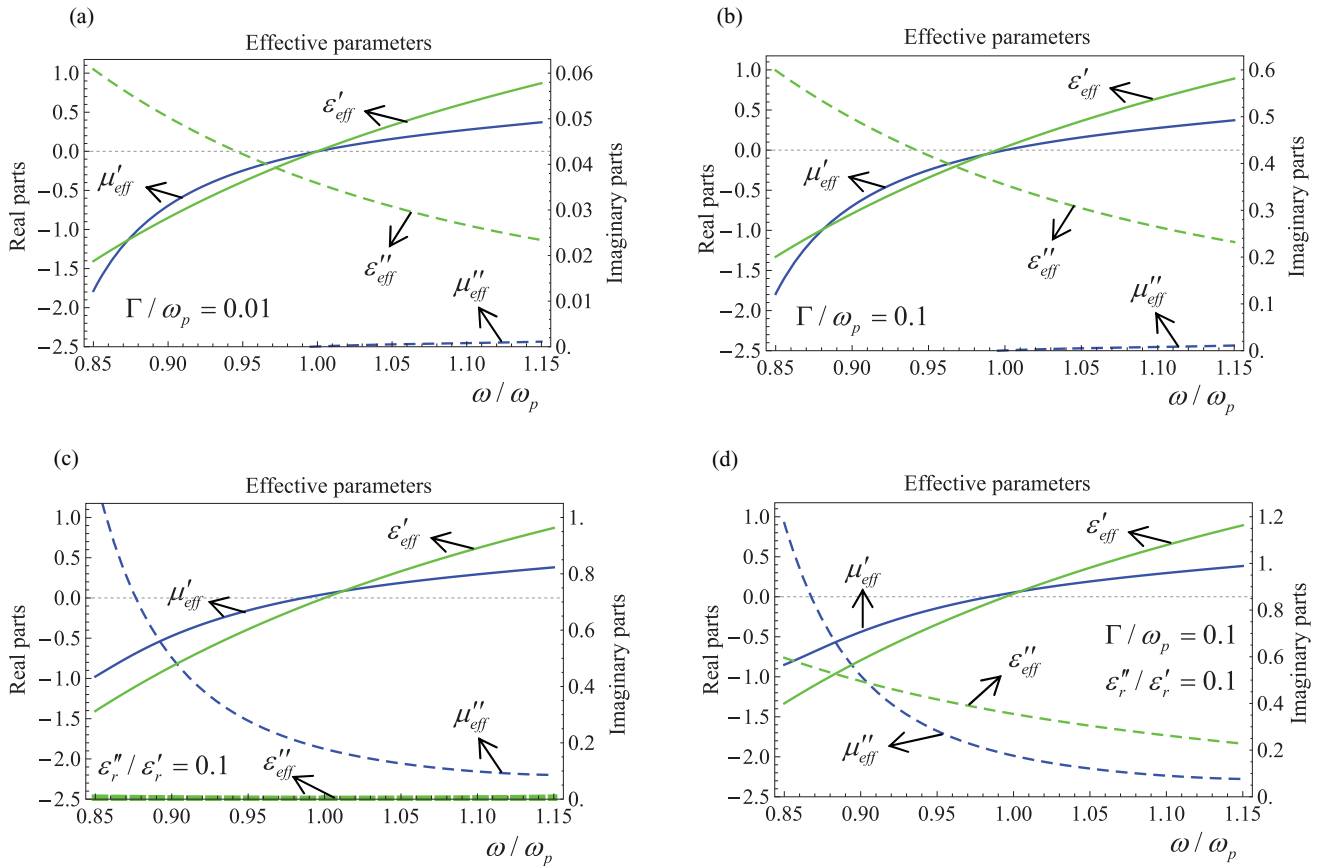
FIG. 3. (Color online) Real and imaginary parts of the effective permittivity $\varepsilon_{\text{eff}} = \varepsilon'_{\text{eff}} + i\varepsilon''_{\text{eff}}$ (green curves) and permeability $\mu_{\text{eff}} = \mu'_{\text{eff}} + i\mu''_{\text{eff}}$ (blue curves) as a function of the normalized frequency ω/ω_p, for the same configuration as in Fig. 2, except that losses are taken into account: (a) $\Gamma/\omega_p = 0.01$. (b) $\Gamma/\omega_p = 0.1$. (c) $\varepsilon''_r/\varepsilon'_r = 0.1$. (d) $\Gamma/\omega_p = 0.1$ and $\varepsilon''_r/\varepsilon'_r = 0.1$. The solid lines correspond to the real parts of ε_{eff} and μ_{eff} while the dashed lines represent the imaginary parts.

band structure is formed by two nearly twin bands that have reflection symmetry with respect to $\omega = \omega_p$, and are associated with transverse electromagnetic waves. The two bands touch at the $k = 0$ point, because the condition $\varepsilon_{\text{eff}} \approx \mu_{\text{eff}} \approx 0$ excludes the possibility of a photonic band gap and ensures a continuous linear dispersion close to the plasma frequency. In Fig. 4(a), the lower band corresponds to the frequency window where the material behaves as a left-handed material, which
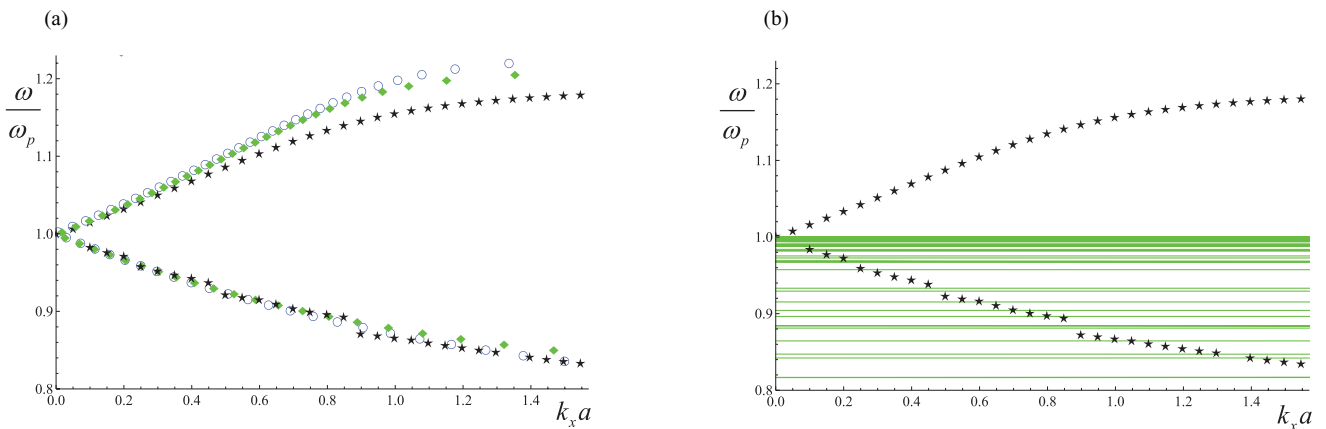

FIG. 4. (Color online) (a) Band structure (only the bands associated with transverse electromagnetic waves are shown) calculated from: full-wave homogenization (Ref. 11) (blue circles); Clausius–Mossotti formula (green diamonds); plane wave method (black stars). (b) The complete band structure calculated using the plane wave method, showing also the dispersionless bands associated with the longitudinal modes (the dispersion of the transverse modes is plotted with black stars so that it can be distinguished from the dispersion of the longitudinal modes).

in this case happens for $0.85 < \omega/\omega_p < 1.0$. The negative slope of this band shows that the group velocity $v_g = \frac{\partial \omega}{\partial k}$ is negative for $0.85 < \omega/\omega_p < 1$, confirming the emergence of backward wave propagation in this regime. On the other hand, the upper band corresponds to a frequency window where both $\varepsilon_{\text{eff}}(\omega)$ and $\mu_{\text{eff}}(\omega)$ are positive (right-handed material), which happens for $1 < \omega/\omega_p < 1.23$.

Besides the two bands associated with the transverse modes, there are also two flat bands at $\omega = \omega_p$ [not shown in Fig. 4(a)] which are associated with longitudinal modes. The emergence of such plasmon modes is made possible by the condition $\varepsilon_{\text{eff}} \approx \mu_{\text{eff}} \approx 0$. The electric plasmon modes are such that **E** is parallel to the wave vector and **H** = 0 and occur when $\varepsilon_{\text{eff}} = 0$. Similarly, the magnetic plasmon modes are such that **H** is parallel to the wave vector and **E** = 0 and occur when $\mu_{\text{eff}} = 0$.

To further validate the extracted effective parameters, we have calculated the exact band structure of the periodic medium using the plane wave method.[18] Since the host material is dispersive, the plane wave method must be implemented as described in Refs. [19–22]. To ensure the convergence of the plane wave method, we had to expand the (in-plane) electric field into 2148 plane waves. The computed results [along a segment of the Brillouin zone with **k** = $(k_x, 0)$] are depicted in Fig. 4(b). As seen, the band structure is formed by a very large number of nearly dispersionless (flat) bands with accumulation point at $\omega = \omega_p$. Such bands correspond to the longitudinal plasmon modes discussed previously. For an ideal continuous medium, they should all be concentrated at $\omega = \omega_p$, but due to the granularity of the structure, this is not strictly observed in the metamaterial implementation. It is worth noting that there is an infinite number of flat bands because, due to the periodicity of the structure, the plasmon band is folded into many branches.

Besides the dispersionless bands, it is possible to identify in Fig. 4(b) two nearly twin bands [black stars in Fig 4(b), also depicted in Fig 4(a)], whose dispersion matches well the dispersion of the transverse electromagnetic waves computed with homogenization theory [Fig. 4(a)]. Therefore, the band structure calculations support the effective medium theory.

The described ideas can be readily generalized to the three-dimensional case. To illustrate this, we consider an array of spheres with permittivity ε_r, embedded in a near-zero permittivity host, and arranged in a cubic lattice with lattice constant a (see the inset of Fig. 5). It has been shown in previous works that arrays of magneto-dielectric spheres standing in air enable a DNG response;[23] however, the difference in our design is that the spheres have no intrinsic magnetic response and are embedded in a plasmonic material.

It was shown recently with full-wave homogenization simulations that the metamaterial response can be accurately modeled using the Lewin's formulas when the inclusions are embedded in a low permittivity host.[24] For the case of inclusions with trivial permeability, the Lewin's formulas read:[25]

$$\varepsilon_L = \varepsilon_h \left(1 + \frac{1}{a^3 \alpha_e^{-1} - 1/3}\right), \quad \mu_L = 1 + \frac{1}{a^3 \alpha_m^{-1} - 1/3} \quad (1)$$
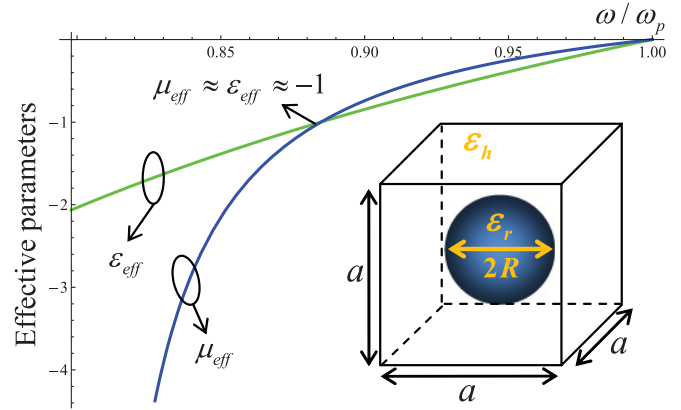

FIG. 5. (Color online) Effective permittivity ε_{eff} (green curves) and permeability μ_{eff} (blue curves) ($\Gamma/\omega_p = 0$) as a function of the normalized frequency ω/ω_p. Both curves were calculated using Lewin's formulas. The geometry of the unit cell is shown in the inset: it consists of a spherical inclusion with normalized radius R/a and permittivity ε_r embedded in a host medium with permittivity ε_h described by a Drude-type dispersion model.

where

$$\alpha_e^{-1} = \frac{1}{4\pi R^3} \frac{F(\theta) + 2\varepsilon_h/\varepsilon_d}{F(\theta) - \varepsilon_h/\varepsilon_d}, \quad \alpha_m^{-1} = \frac{1}{4\pi R^3} \frac{F(\theta) + 2}{F(\theta) - 1}. \quad (2)$$

with $F(\theta) = \frac{2(\sin\theta - \theta\cos\theta)}{(\theta^2 - 1)\sin\theta + \theta\cos\theta}$ and $\theta = (\omega R/c)\sqrt{\varepsilon_d}$. In the previous formulas, ε_d is the permittivity of the spherical inclusions and ε_h the permittivity of the host material.

To investigate the potentials of this fully three-dimensional (3D) configuration, we consider first that the plasma frequency is such that $\omega_p a/c = 1.0$ and that $\Gamma/\omega_p = 0$ (lossless case). The normalized radius of the spheres is $R/a = 0.482$ and the dielectric permittivity $\varepsilon_r \approx 58.4$. These parameters ensure a matched DNG operation $\varepsilon_{\text{eff}}(\omega) \approx \mu_{\text{eff}}(\omega)$. The effective parameters calculated with Lewin's theory [Eq. (1)] are depicted in Fig. 5, showing a very wideband DNG response in the range $0.8 < \omega/\omega_p < 1.0$ and that $\varepsilon_{\text{eff}}(\omega) \approx \mu_{\text{eff}}(\omega) \approx -1$ at $\omega a/c = 0.88$, in qualitative agreement with the results for the 2D configuration.

Next, we investigate the sensitivity to loss of the 3D configuration. In Fig. 6(a), losses in the host medium are taken into account by setting the damping frequency to $\Gamma/\omega_p = 0.01$. Similar to the 2D case, the 3D configuration remains tuned when the host medium is lossy, as the effective parameters $\varepsilon_{\text{eff}}(\omega)$ and $\mu_{\text{eff}}(\omega)$ are matched and simultaneously negative in a broad frequency band of operation. Lewin's formulas [Eqs. (1) and (2)] predict that the effective magnetic permeability μ_{eff} is not affected by the dielectric response of the host medium, and accordingly, in Fig. 6(a), the imaginary part of the magnetic permeability $\mu_{\text{eff}} = \mu'_{\text{eff}} + i\mu''_{\text{eff}}$ is zero valued in the whole spectral range. This behavior is qualitatively consistent with the results obtained with the full-wave homogenization method for the 2D configuration. The results reported in Figs. 6(b), 6(c), and 6(d) are also qualitatively analogous to those reported in Figs. 3(b), 3(c), and 3(d), where it was seen that even in the presence of strong loss in both the host medium and dielectric inclusions, the effective response of the 3D configuration remains very broadband, even in the worst
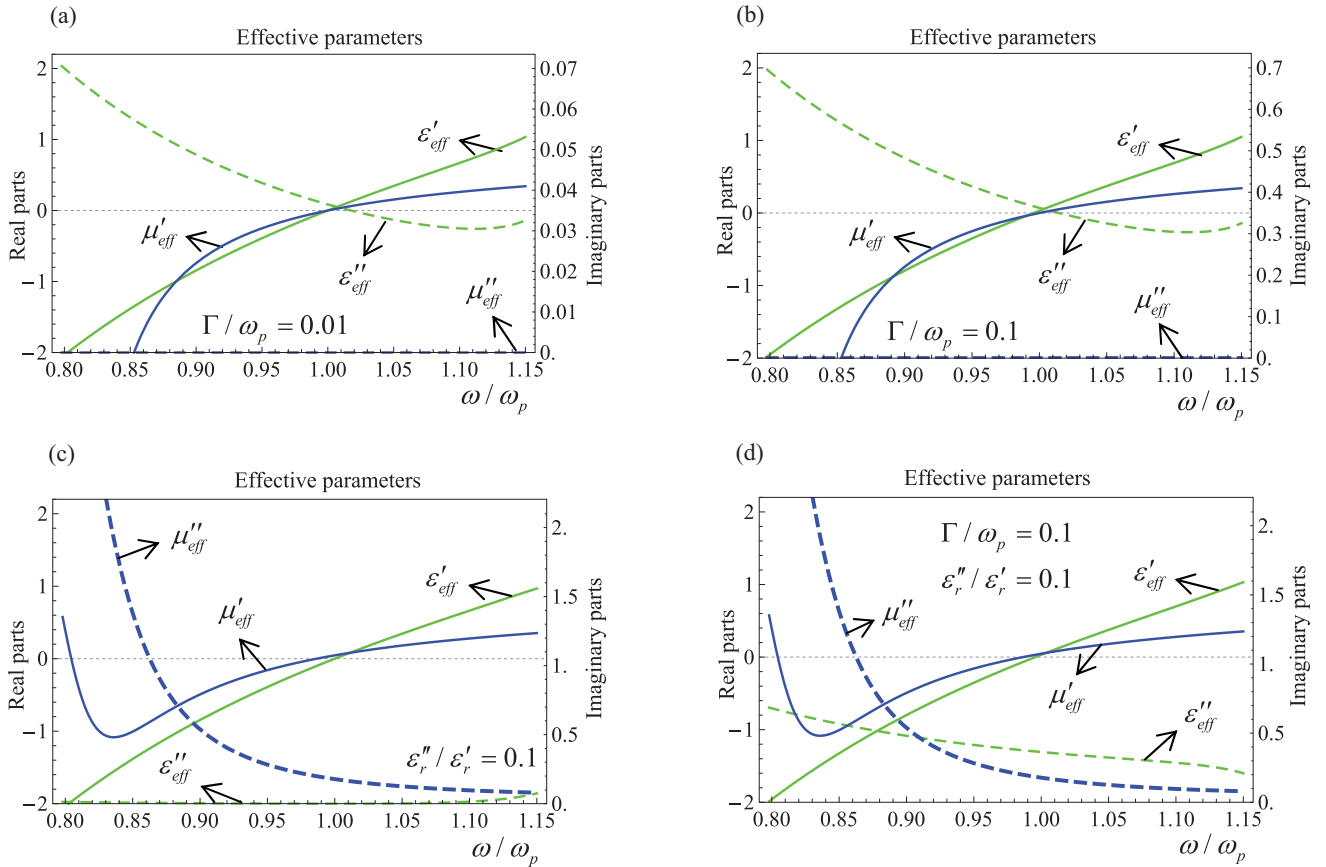
FIG. 6. (Color online) Real and imaginary parts of the effective permittivity $\varepsilon_{\text{eff}} = \varepsilon'_{\text{eff}} + i\varepsilon''_{\text{eff}}$ (green curves) and permeability $\mu_{\text{eff}} = \mu'_{\text{eff}} + i\mu''_{\text{eff}}$ (blue curves) as a function of the normalized frequency ω/ω_p, for the same configuration as in Fig. 5, except that losses are taken into account: (a) $\Gamma/\omega_p = 0.01$. (b) $\Gamma/\omega_p = 0.1$. (c) $\varepsilon''_r/\varepsilon'_r = 0.1$. (d) $\Gamma/\omega_p = 0.1$ and $\varepsilon''_r/\varepsilon'_r = 0.1$. The solid lines correspond to the real parts of ε_{eff} and μ_{eff}, while the dashed lines represent the imaginary parts.

scenario [Fig. 6(d)], where both host medium and inclusions are simultaneously affected by strong loss modeled by $\Gamma/\omega_p = 0.1$ and $\varepsilon''_r/\varepsilon'_r = 0.1$.

To conclude this section, we discuss possible combinations of realistic materials that may enable realizing the described metamaterial. At infrared and optical frequencies, the role of the plasmonic material may be played (at very specific frequency bands) either by noble metals (e.g. silver in the optical regime) or polar dielectrics (e.g. SiC at the far-IR).[26] However, in these regimes, materials with large permittivities are difficult to find, even though they may be possibly synthesized as metamaterials.[27] Yet, the most promising possibility is perhaps the terahertz regime, where several materials with high index and relatively low loss are readily available (e.g. TiO₂, MgO:LiNbO₃).[28,29] In this regime, either materials with a terahertz polariton resonance, such as CsI,[30] or semiconductors (e.g. InSb)[31] are characterized by a negative permittivity in some frequency band and thus may be used as the host material.

As an example, here we consider a 3D setup based on TiO₂ (titanium dioxide) spheres embedded in an HgTe (mercury telluride) host. HgTe is a high-mobility (degenerate) semiconductor, whose electrical response may be modeled by a Drude model of the form $\varepsilon(\omega) = \varepsilon_\infty[1 - \frac{\omega_p^2}{\omega(\omega + i\Gamma)}]$, with plasma frequency $\omega_p = \sqrt{\frac{Ne^2}{m^* \varepsilon_\infty \varepsilon_0}}$ and collision frequency $\Gamma = \frac{e}{m^* \mu_n}$ (within the same level of approximation as that considered in Ref. 31 for InSb), where $-e$ is the electron charge, and ε_0 is the permittivity of vacuum. With the data available in the literature, it is possible to estimate that $\varepsilon_\infty = 14.4$[32] and that the effective electron mass is $m^* = 0.03m_0$.[33] On the other hand, the mobility of the electrons μ_n and the electron concentration N depend significantly on the temperature and can be calculated using the data of Refs. 34 and 35. As a consequence, the plasma and collision frequencies of HgTe are tunable with the temperature. At room temperature, we have $\mu_n \approx 3.5 \times 10^3$ cm²V/s and $N \approx 4.3 \times 10^{17}$ cm⁻³, and thus the plasma frequency should be about $\omega_p/2\pi = 9.0$ [THz] and the collision frequency $\Gamma/2\pi = 0.27$ [THz]. Unfortunately, this value of ω_p is far too high to enable the combination of HgTe and TiO₂ at room temperature in our design. Indeed, after the polaritonic resonance of TiO₂ at 5.7 THz, its permittivity drops sharply.[28] To circumvent this problem, we will consider operation at lower temperatures to effectively decrease the plasma frequency of HgTe. The permittivity of TiO₂ is almost insensitive to temperature.[28]
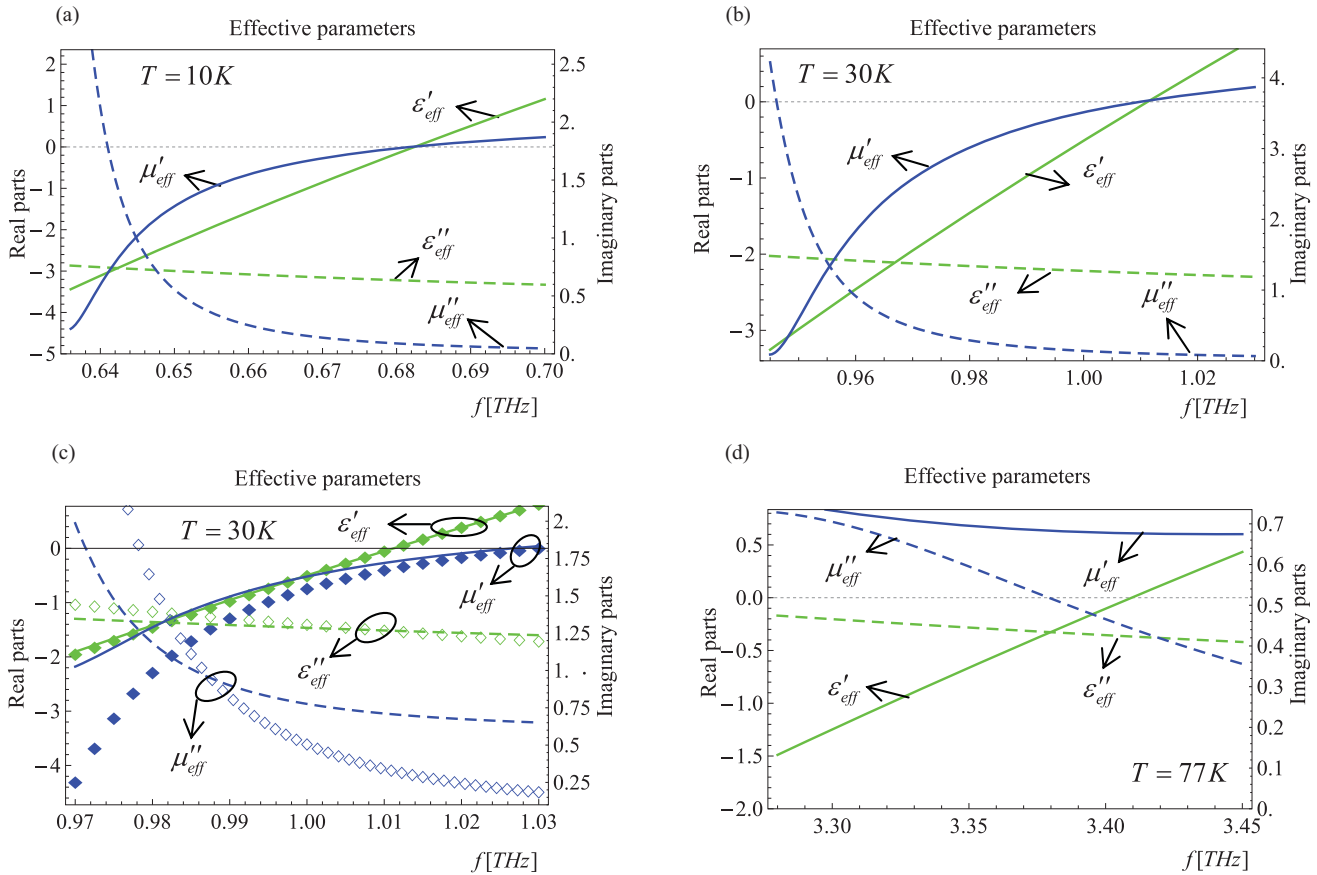
FIG. 7. (Color online) Real and imaginary parts of the effective permittivity $\varepsilon_{\text{eff}} = \varepsilon'_{\text{eff}} + i\varepsilon''_{\text{eff}}$ (green curves) and permeability $\mu_{\text{eff}} = \mu'_{\text{eff}} + i\mu''_{\text{eff}}$ (blue curves) as a function of frequency in the terahertz domain, for the scenario wherein the plasmonic host is HgTe and the spherical inclusions are made of TiO$_2$. (a) $T = 10$ K. (b) $T = 30$ K. (c) Similar to (b), but the radius of the TiO$_2$ was tuned to ensure that $\varepsilon'_{\text{eff}} \approx \mu'_{\text{eff}} \approx -1$ at $f = 0.989$ THz. The discrete symbols were calculated using the full-wave homogenization (Ref. 24), and the solid curves were determined using Eqs. (1) and (2). (d) $T = 77$ K.

In the first example [Fig. 7(a)], we consider operation at $T = 10$ K for which the plasma frequency of HgTe can be estimated as $f_p \approx 0.683$ THz. The permittivity of TiO$_2$ at this frequency is $\varepsilon_{\text{TiO}_2} \approx 93.9 + i1.3$.[28] In order to ensure $\varepsilon_{\text{eff}} \approx \mu_{\text{eff}} \approx 0$ at $f = 0.683$ THz, we use Eqs. (1) and (2) to determine the radius of the spheres, and this yields $R/a = 0.35$ ($a = 70.0$ μm). The results shown in Fig. 7(a) confirm that the effective response of the 3D configuration formed by realistic materials may provide a fairly matched and fairly broadband DNG response, i.e. the real part of the effective permittivity $\varepsilon'_{\text{eff}}$ (solid green curve) is reasonably identical to the real part of the effective magnetic permeability μ'_{eff} (solid blue curve) in a relatively wide range of frequencies. The bandwidth of DNG operation is about 8%, which should be contrasted with the results of Sec. II. It is relevant to mention that it is possible to achieve a bandwidth of DNG operation of nearly 10% with metamaterials formed by split ring resonators and metallic wires,[36] a bandwidth of about 20% with metamaterials formed by several layers of fishnets,[37] or even larger values using transmission line based metamaterials.[38] Nevertheless, these structures do not provide an isotropic matched local response, unlike our metamaterial, or may require electronic lumped components not available at optics.

The effective parameters were also determined for a temperature $T = 30$ K [Fig. 7(b)]. In this scenario, the plasma frequency of HgTe may be estimated as $f_p \approx 1.012$ THz and $\varepsilon_{\text{TiO}_2} \approx 95.2 + i2.0$. The normalized radius of the TiO$_2$ spheres is chosen as $R/a = 0.34$ ($a = 47.2$ μm). The behavior of the effective parameters is identical to that of Fig. 7(a) but with a shift in frequency, as a consequence of the temperature increase. It should be noticed that even though the effective response remains broadband at $T = 30$ K, the matching properties are slightly deteriorated. In order to have simultaneously $\varepsilon = -1$ and $\mu = -1$ the radius of the spheres may be slightly decreased to $R/a = 0.33$ [Fig. 7(c)]. It can be seen in Fig. 7(c) that this provides $\varepsilon'_{\text{eff}} \approx \mu'_{\text{eff}} \approx -1$ at $f \approx 0.989$ THz. In Fig. 7(c), we also depict the effective parameters calculated using a time-domain full-wave homogenization,[24] confirming the accuracy of the Lewin's formulas.[25] Finally, in Fig. 7(d), the effective response of the 3D configuration is depicted at $T = 77$ K. For this temperature, $f_p \approx 3.411$ THz and $\varepsilon_{\text{TiO}_2} \approx 136.5 + i14.7$. The normalized radius of the spheres is chosen $R/a = 0.276$ ($a = 78.2$ μm). It can be seen [Fig. 7(d)] that at 77 K it is not possible anymore to ensure a DNG response. In fact, the effective magnetic response is strongly damped by the increased loss of TiO$_2$ (due to operation closer

to the resonance of TiO$_2$) because, as discussed previously, the effective magnetic response is mainly affected by the loss in the dielectric inclusions.

IV. NEGATIVE REFRACTION

To further characterize the potentials of the proposed meta-materials, we studied the refraction of a Gaussian cylindrical beam by a planar metamaterial slab using a commercial full-wave electromagnetic simulator.[39] In the first example, we consider the 2D configuration reported in Sec. III where the inclusions are high-index cylinders and the magnetic field is parallel to the axes of the cylinders (z direction). The metamaterial slab is finite along the x and y directions, with dimensions $L_x = 17.8a$ and $L_y = 60.4a$, respectively. In the simulation, the effect of loss was taken into account by considering that the collision frequency satisfies $\Gamma/\omega_p = 0.05$. The Gaussian beam illuminates the slab along the direction $\theta_i = 33°$. Figure 8(a) shows a snapshot in time of the z component of the magnetic field at $\omega a/c = 0.88$, i.e. at the frequency where, according to the results shown in Fig. 2, the effective parameters are $\varepsilon_{\text{eff}} \approx \mu_{\text{eff}} \approx -1$. The negative refraction is evident from Fig. 8(a), which shows that the beam is bent in an unusual way at the interfaces.

While in the previous configuration, the DNG response is polarization sensitive and is revealed only when the magnetic field is parallel to the cylindrical inclusions, it is possible to overcome this limitation by considering spherical inclusions. In such a scenario, we can obtain a magnetic response for the two polarizations, i.e. both when the magnetic field is parallel to the z direction (P-polarized waves) and also when the electric field is parallel to the z direction (S-polarized waves). To illustrate this, we consider a metamaterial formed by spherical dielectric inclusions with dimensions $L_x = 8.87a$ and $L_y = 54.3a$ along the x and y directions, respectively. The metamaterial has the same parameters as in Fig. 5, except that losses in the host material were also taken into account assuming $\Gamma/\omega_p = 0.05$. Figures 8(b) and 8(c) show a snapshot in time of the z component of the magnetic field (for a P-polarized incident wave) and of the electric field (for an S-polarized incident wave), respectively, when the metamaterial is illuminated by a cylindrical Gaussian beam. These two snapshots are calculated at $\omega a/c = 0.88$, the frequency at which the effective parameters satisfy $\varepsilon_{\text{eff}} \approx \mu_{\text{eff}} \approx -1$, and at a $z = $ const. plane that cuts the spheres into two equal parts (i.e. at half height of the unit cell). Nevertheless, it can be checked (not shown here) that the results obtained for other cuts are very similar. The results of Fig. 8(b) and 8(c) confirm a strong negative refraction effect for both polarizations and that the level of reflections is very low, demonstrating that the metamaterial is well matched with free space. It should be noticed that the transmission and incident angles satisfy $\theta_t \approx -\theta_i$, consistent with the fact that $n \approx -1$.

Next, we discuss the effects of disorder on the response of the metamaterial. As demonstrated theoretically in Ref. 14, in the 2D scenario and in the limit of vanishing loss, a wave that illuminates the slab at the plasma frequency cannot distinguish if the slab is a continuous medium (with parameters $\varepsilon_{\text{eff}}(\omega_p) \approx \mu_{\text{eff}}(\omega_p) \approx 0$ in case of a zero-index medium, as considered here) or if it is a metamaterial implementation of the same
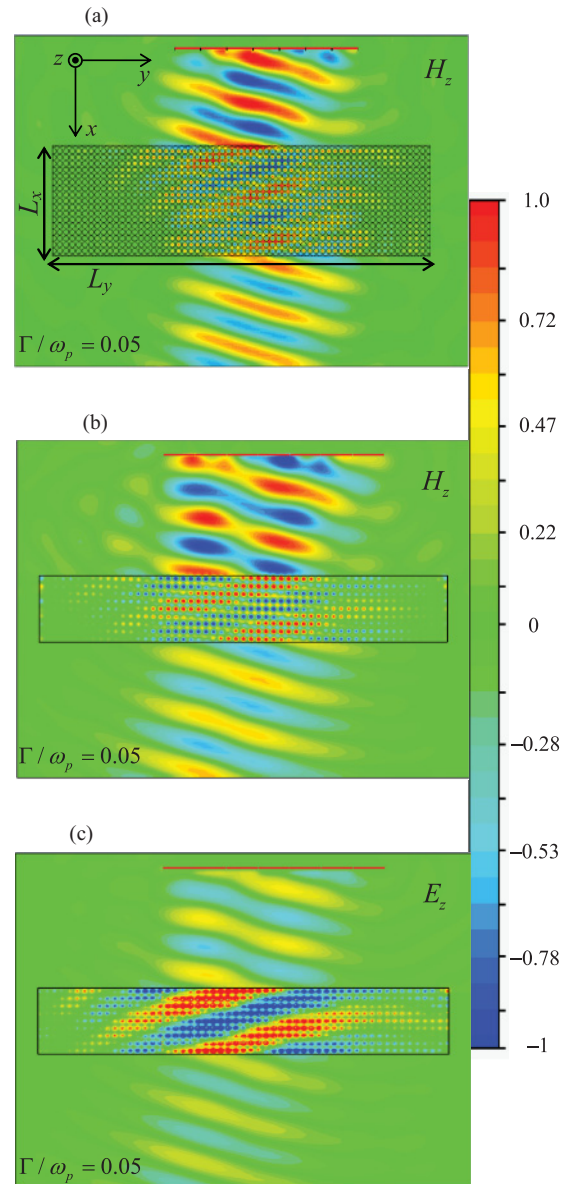

FIG. 8. (Color online) Snapshots of H_z (P-polarized waves) and E_z (S-polarized waves) when a cylindrical Gaussian beam illuminates ($\theta_i = 33°$) a metamaterial slab: (a) 2D configuration (cylindrical inclusions) and slab with dimensions $L_x = 17.8a$ and $L_y = 60.4a$ and plasmonic host with collision frequency $\Gamma/\omega_p = 0.05$. (b) and (c) 3D configuration (spherical inclusions) and a slab with dimensions $L_x = 8.87a$ and $L_y = 54.3a$ and plasmonic host with collision frequency $\Gamma/\omega_p = 0.05$.

medium. Indeed, at the plasma frequency, the electromagnetic fields are unable to sense the granularity of the slab. Moreover, in this ideal scenario, the metamaterial response is also totally insensitive to disorder effects, and an external observer is unable to tell if the inclusions of the metamaterial slab are periodically or randomly arranged.[14,40,41] This is made possible by the fact that the wavelength in the host medium is infinite at $\omega = \omega_p$, and thus the electrical size of the inclusions is very small, independent of their actual physical size. Even though this property is rigorously valid only when
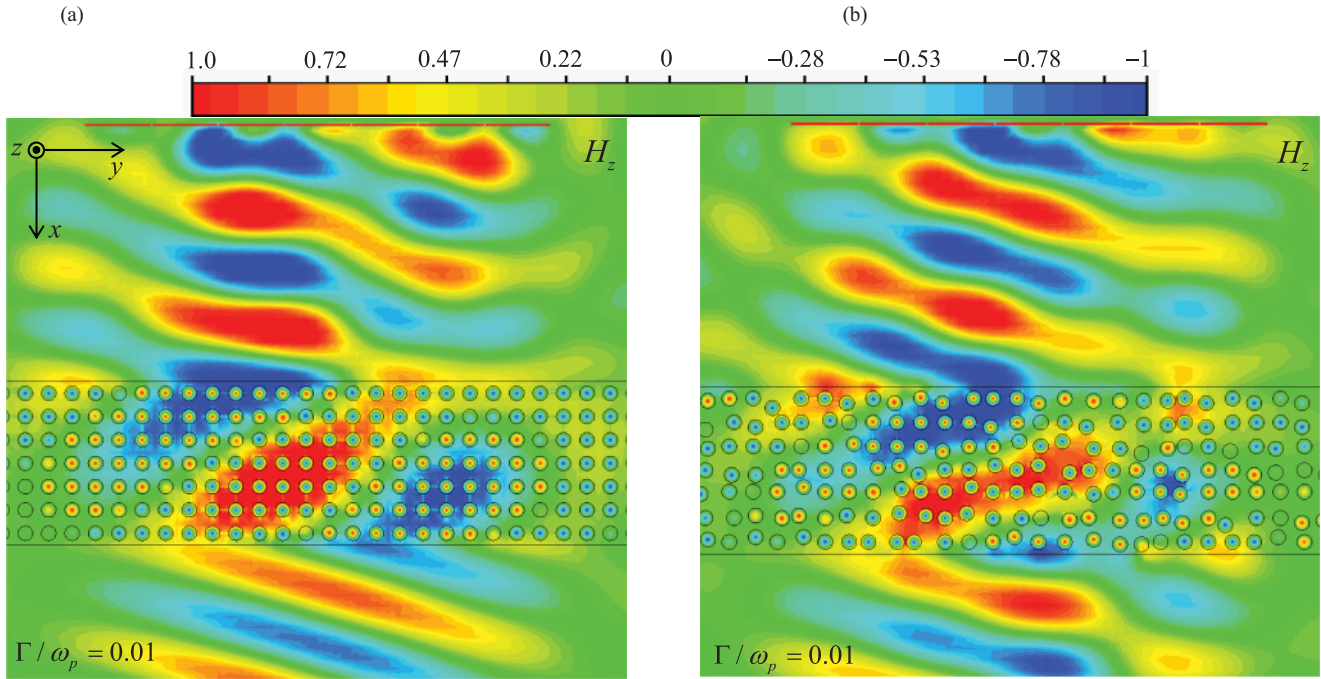
FIG. 9. (Color online) Snapshots of H_z when a Gaussian beam illuminates a metamaterial slab formed by cylindrical inclusions ($\theta_i = 33°$). (a) Slab with dimensions $L_x = 7a$ and $L_y = 60a$ composed by an array of cylinders arranged in a square lattice within a plasmonic host with collision frequency $\Gamma/\omega_p = 0.01$. (b) Similar to (a), but the cylinders are randomly positioned within the host.

$\omega = \omega_p$, it remains approximately valid at nearby frequencies. To demonstrate this, we studied the effect of positional disorder on the refraction of waves by a metamaterial slab formed by cylindrical inclusions. The dimensions of the slab in this example are $L_x = 7a$ and $L_y = 60a$. In order to have a higher degree of disorder, we have reduced the radius of the inclusions to $R/a = 0.315$ and increased the plasma frequency to $\omega_p a/c = 1.66$, compared to the previous examples. The dielectric permittivity ($\varepsilon_r \approx 39.12$) was tuned so that at $\omega a/c \approx 1.33$ the effective permeability and permittivity satisfy $\varepsilon_{\text{eff}} \approx \mu_{\text{eff}} \approx -1$. The effect of loss was taken into account by using $\Gamma/\omega_p = 0.01$. Figures 9(a) and 9(b) show a snapshot in time of the magnetic field when the inclusions are periodically and randomly arranged, respectively (the specific spatial arrangement of the inclusions in the two cases can be seen directly in Fig. 9). It is clear [also from the time animation of Fig. 9(b) reported in Ref. 42], consistent with the previous discussion, that the response of the metamaterial and the negative refraction are little affected by disorder of the structure, confirming that the incident beam is unable to sense the granularity of the metamaterial. Notice that when $\varepsilon_{\text{eff}} \approx \mu_{\text{eff}} \approx -1$, the real part of the permittivity of the host is $\varepsilon_h \approx -0.56$, and thus the contrast between the permittivity of the host and inclusions is near zero ($\varepsilon_h/\varepsilon_d \approx -0.01$), as required in order that the theory of Ref. 14 applies.

Next, we investigate the possibility of achieving negative refraction in a 3D-configuration wherein the host medium is HgTe and the spherical inclusions are made of TiO$_2$, with the same parameters as in the example of Fig. 7(c). The dimensions of the slab are $L_x = 3.84a$ and $L_y = 44.3a$ along the x and y directions, respectively ($a = 47.2\ \mu$m). Figures 10(a) and 10(b) show a snapshot in time of the z component of the electric field (for an S-polarized incident wave) and of the magnetic field (for

a P-polarized incident wave), respectively, at $f = 0.989$ THz, the frequency at which $\varepsilon'_{\text{eff}} \approx \mu'_{\text{eff}} \approx -1$. Despite the presence of loss both in the host medium and dielectric, the negative refraction is well evident in the figures and also in the time animations.[43,44]

V. SUPERLENSING

One of the most exciting potentials of DNG materials is the fact that a metamaterial slab with $\varepsilon_{\text{eff}} \approx \mu_{\text{eff}} \approx -1$ is able to suppress the effects of diffraction and focus electromagnetic radiation with no limit of resolution.[2] Unlike conventional optical lenses, which can only process the propagating waves, a DNG slab permits restoring the evanescent waves. In the near field, the condition $\varepsilon_{\text{eff}} \approx \mu_{\text{eff}} \approx -1$ can be relaxed, and there are simpler solutions to achieve superlensing.[45–48] Indeed, to obtain superlensing for a specific polarization, it is sufficient to guarantee that only one of the effective parameters (ε_{eff} or μ_{eff}) is negative. This is a result of the almost total decoupling between the magnetic and electric responses in the near field.

It is natural to wonder if the metamaterial structures investigated in previous sections may mimic to some extent the response of the perfect lens. To this end, first, we consider the configuration where the metamaterial is formed by cylindrical inclusions and has the same parameters as in Fig. 2. Using a full wave electromagnetic simulator,[39] we determined the transfer function T of a metamaterial slab as a function of the transverse wave number of the impinging wave, k_y. The frequency of operation is $\omega a/c = 0.88$, i.e. the frequency at which the effective parameters of the metamaterial satisfy $\varepsilon_{\text{eff}} \approx \mu_{\text{eff}} \approx -1$. The slab has dimensions $L_x = a$, and it is infinite along the y and z directions, and the effect of loss was taken into account supposing that the collision frequency of the plasmonic host
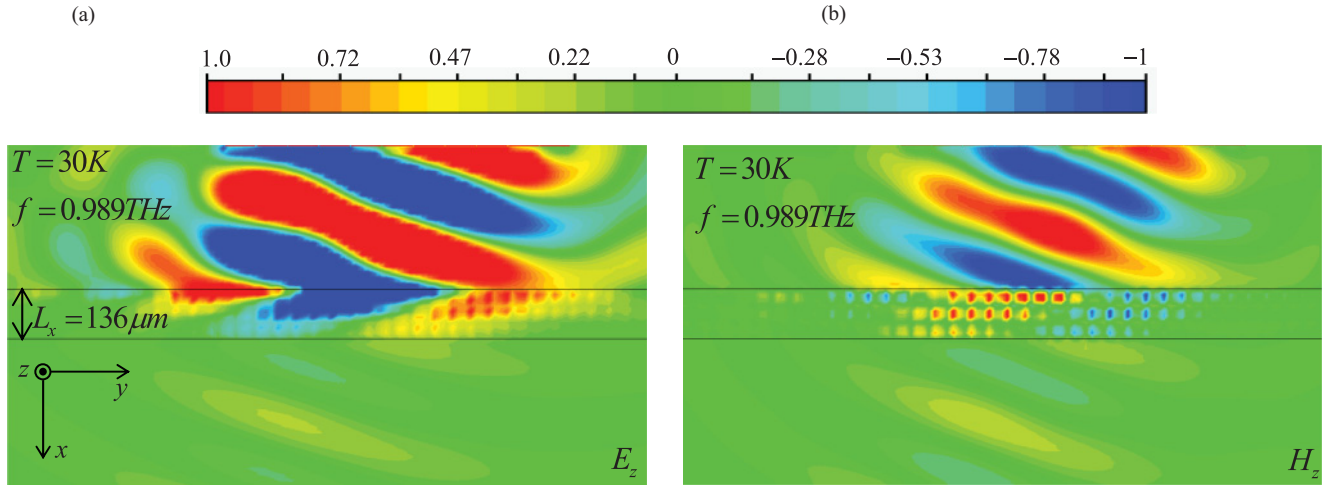
(a)   (b)

FIG. 10. (Color online) Snapshots of the electromagnetic fields when a Gaussian beam ($\theta_i = 22°$) illuminates a metamaterial slab formed by TiO$_2$ spherical inclusions embedded in a HgTe host, with dimensions $L_x = 3.85a$ and $L_y = 44.3a$. (a) S-polarized waves. (b) P-polarized waves.

is such that $\Gamma/\omega_p = 0.01$. The obtained results are depicted in Fig. 11 (blue solid curve) and are compared with the transfer function of an ideal Pendry's lens (black dashed curve) with $\varepsilon = \mu = -1$ ($T = e^{\gamma_0 L_x}$, with $\gamma_0 = \sqrt{k_y^2 - (\omega/c)^2}$). As seen, the results are qualitatively similar, and support, undoubtedly, that the metamaterial indeed amplifies the evanescent waves (i.e. waves with $k_y c/\omega > 1$). We would like to point out that the edge of the Brillouin zone ($k_y a = \pi$) corresponds in Fig. 11 to $k_y/k_0 = \pi/0.88 = 3.57$, i.e. to the range of the horizontal axis. Thus, as expected, the resolution of the system is ultimately limited by the granularity of the material.

Using CST Microwave Studio,[39] we simulated the case wherein a magnetic line source (infinitely extended along the z direction) [see inset of Fig. 12(a)][49] is placed at a distance d_1 above the metamaterial slab. The slab has the
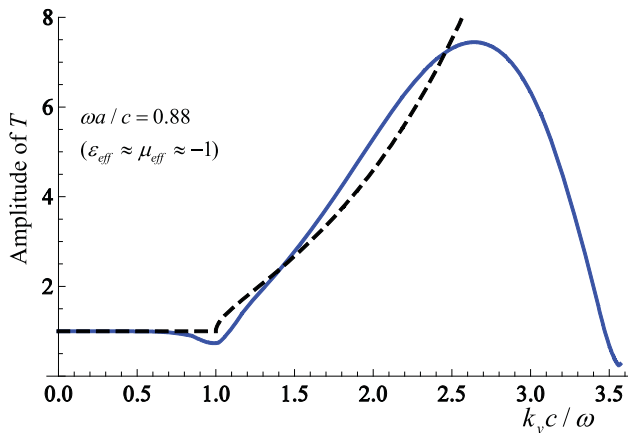

FIG. 11. (Color online) Amplitude of the transfer function T of the metamaterial slab as a function of the transverse wave vector, k_y, for a fixed frequency of operation ω. The slab has dimensions $L_x = a \approx 0.14\lambda_0$ and is infinite along the y and z directions. The blue solid line was obtained with a full-wave simulation using CST Microwave Studio (Ref. 39), whereas the black dashed line represents the transfer function of an ideal Pendry's lens with $\varepsilon \approx \mu \approx -1$.

same parameters as in Fig. 11, but it is finite along the y direction with $L_y = 30.55a$. The magnetic field profile was calculated at a plane located at a distance d_2 below the slab. It was assumed that $d_1 = d_2 = 0.5L_x = 0.07\lambda_0$. Notice that the slab thickness corresponds to a single period of the bulk metamaterial. In principle, unlike in other configurations reported in the literature, this will not invalidate the effective medium approximation, because when the permittivity of the host material is near zero, the electromagnetic wave that illuminates the material slab may see the material as a continuous material, independent of the exact thickness of the material in the direction of propagation[14] (this property may, however, not hold when the excitation is placed in the very near field of the slab due to the excitation of higher-order diffraction modes).

The normalized magnetic field at the image plane is depicted in Fig. 12(a) as a function of y/λ_0 (solid blue curve), where λ_0 is the wavelength associated with the frequency of operation that provides $\varepsilon_{\text{eff}} \approx \mu_{\text{eff}} \approx -1$. The half-power beamwidth (HPBW) is equal to $0.2\lambda_0$. The square normalized magnetic field at the image plane, when the slab is absent and the distance between the source and the image plane is $d_1 + d_2$, is also shown in Fig. 12(a) (dashed blue curve). It should be noticed that, when the lens is present, the total distance between the source and the image plane is $d_1 + d_2 + L_x = 0.28\lambda_0$; whereas when the lens is absent, the distance is reduced to $d_1 + d_2 = 0.14\lambda_0$. Thus, notwithstanding the greater proximity between the source and the image plane, in the latter case, the HPBW increases to $0.3\lambda_0$. For the propagating distance $d_1 + d_2 + L_x$ in free space, the HPBW is $0.48\lambda_0$. It is clear that the metamaterial lens enables, indeed, a superlensing effect and compensates the effects of propagation of free space.

Figure 12(b) shows the square normalized magnetic field as a function of the distance d_2 of the image plane to the slab interface. The solid curves correspond to the magnetic fields calculated in the presence of lens, whereas the dashed curves represent the same but when the lens is absent and the propagation distance in air is $d_1 + d_2$. It is seen that the transmitted beam remains significantly narrower than the beam radiated by the source in free space, even for large
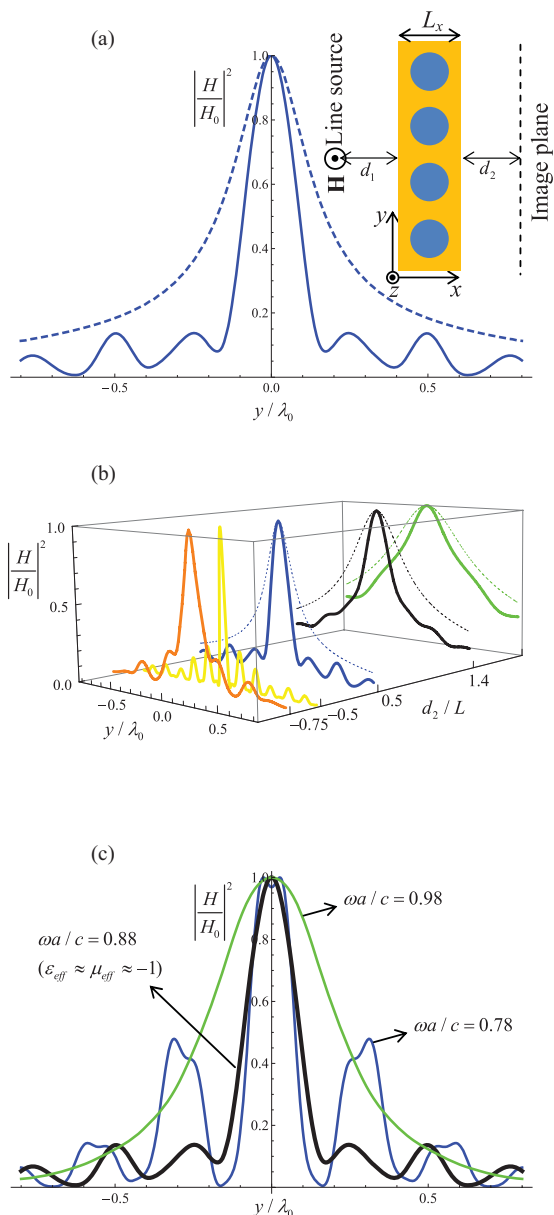
FIG. 12. (Color online) Profiles of the fields for a magnetic line source placed at a distance $d_1 = 0.5L_x$ above the superlens. The image plane is located at a distance $d_2 = d_1$ from the lower interface of the lens. (a) Square normalized amplitude of the field imaged by the superlens for a material slab formed by high-index cylindrical inclusions embedded in a plasmonic host; the slab has dimensions $L_x = a \approx 0.14\lambda_0$ and $L_y = 60a$ (solid blue line). The effective parameters at the frequency of operation are such that $\varepsilon_{\mathrm{eff}} \approx \mu_{\mathrm{eff}} \approx -1$. Blue dashed line: the same but without lens. The inset represents the geometry of the problem. (b) Square normalized field profiles as a function of the distance d_2 to the outer interface of the lens. (c) Similar to (a) but for different frequencies of operation.

values of d_2, confirming that the metamaterial slab reverses to some extent the effects of diffraction, consistent with the transfer function of Fig. 11. Notice that in Fig. 12(b) the solid yellow line represents the field profile at the midplane of the metamaterial slab. Clearly, the field is focused inside the lens as a consequence of the negative refraction and of the property $n \approx -1$.

We also studied the imaging properties of the lens when the frequency of operation is detuned from the value $\omega a/c = 0.88$ (frequency where the effective parameters are $\varepsilon_{\mathrm{eff}} \approx \mu_{\mathrm{eff}} \approx -1$) [Fig. 12(c)]. As seen, at a lower frequency of operation $\omega a/c = 0.78$ (solid blue curve), Fig. 12(c) shows that, even though some side lobes may be present, the beam is still sharply focused with the same HPBW as that obtained at $\omega a/c = 0.88$, indicating a reasonable tolerance to the effects of frequency dispersion. However, at $\omega a/c = 0.98$ (solid green line), the lens loses completely its focusing ability.

Next, we investigate the performance of a fully 3D metamaterial slab, such that at the microscopic level it is formed by dielectric spheres embedded in the plasmonic host. We aim to demonstrate that such a configuration (for sufficiently weak loss) may provide superlensing, independent of the wave polarization. Using Microwave Studio,[39] we ran a simulation similar to that of Fig. 12(a) but assuming that the inclusions are dielectric spheres. The metamaterial parameters are as in Fig. 5. The dimensions of the slab in the x and y directions are exactly the same as those considered in Fig. 12(a). It was assumed that $d_1 = d_2 = 0.5L_x = 0.07\lambda_0$, where λ_0 is the wavelength associated with the frequency where the effective parameters are $\varepsilon_{\mathrm{eff}} \approx \mu_{\mathrm{eff}} \approx -1$. In Fig. 13(a), we compare the profile of the magnetic field at the image plane obtained using (i) 2D metamaterial considered in Fig. 12 (solid green line) and (ii) 3D metamaterial (solid blue line) at the frequencies where the effective parameters of both configurations are $\varepsilon_{\mathrm{eff}} \approx \mu_{\mathrm{eff}} \approx -1$. Notice that the wave is P polarized. Interestingly, the HPBW obtained using the spherical inclusions is precisely the same as the one obtained using cylindrical inclusions, and it is equal to $0.2\lambda_0$.

To test whether the 3D configuration is able to work as a superlens for S-polarized waves, we simulated the scenario wherein an electric source (infinitely extended along the z direction) is placed at a distance d_1 above the metamaterial.[50] The slab has dimensions $L_x = a$ and $L_y = 30.55a$ [see the inset of Fig. 13(b)]. The normalized electric field at the image plane is depicted in Fig. 13(b) as a function of y/λ_0 (solid blue line), where λ_0 is the wavelength associated with the frequency of operation where $\varepsilon_{\mathrm{eff}} \approx \mu_{\mathrm{eff}} \approx -1$. The half-power beamwidth (HPBW) is equal to $0.19\lambda_0$, which is slightly narrower than in the case of P-polarized waves. This is only possible because of the strong magnetic response of the metamaterial, since it is well know that the near-field imaging of P-polarized waves requires $\varepsilon \approx -1$, whereas the near-field imaging of S-polarized waves requires $\mu \approx -1$. The square normalized electric field at the image plane when the slab is absent and the distance between the source and the image plane is $d_1 + d_2$ is also shown in Fig. 13(b) (dashed blue curve). Again, notwithstanding the greater proximity between the source and the image plane, in the latter case, the HPBW increases to $0.25\lambda_0$.

In order to further characterize the imaging potential of the 3D-metamaterial slab, we simulated the case where it images the field diffracted by a perfectly conducting screen with two narrow slits (running along the z direction) under plane wave incidence ($\mathbf{E}^{\mathrm{inc}} = E\hat{z}$). The wave diffracted by the slits is thus S polarized. The slits are separated by a distance $d_{\mathrm{gap,slits}} = 0.48\lambda_0$, and the slab has exactly the same parameters as those we used in the example of Fig. 13(b). Figure 13(c) shows the profile of the electric field at the image plane ($d_2 = d_1$) as a
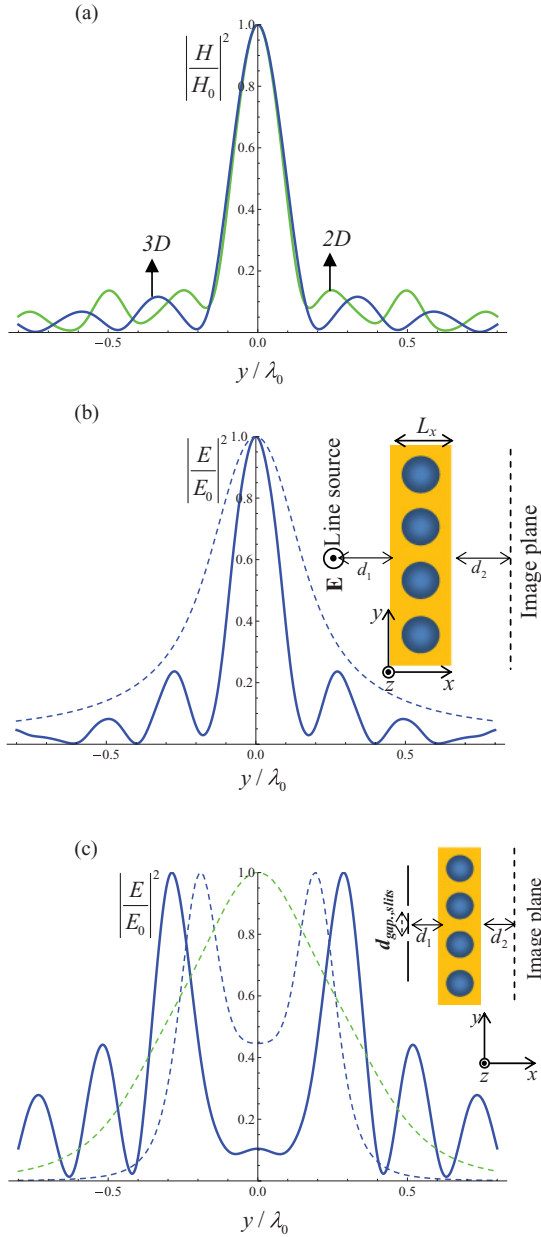
(a)

(b)

(c)

FIG. 13. (Color online) (a) Profile of the square normalized magnetic field for a magnetic line source placed at a distance $d_1 = 0.5L_x$ above the superlens for (i) 2D-configuration (solid green curve) and (ii) 3D-configuration (solid blue curve). (b) Profiles of the electric field for an electric line source placed at a distance $d_1 = 0.5L_x$ above the superlens (3D configuration). The solid blue curve is the profile of the field when the lens is present and at a distance $d_1 + d_2 + L_x = 0.28\lambda_0$ of the electric line source, whereas the dashed blue curve is the profile of the field when the lens is absent and at a distance $d_1 + d_2 = 0.14\lambda_0$ of the electric source. (c) Profile of the electric field diffracted by two narrow slits separated by a distance $d_{\text{gap,slits}} = 0.48\lambda_0$ when the lens is present and at a distance $d_1 + d_2 + L_x = 0.28\lambda_0$ from the slits (blue solid curve); when the lens is absent and at a distance $d_1 + d_2 + L_x = 0.28\lambda_0$ from the slits (green dashed curve); when the lens is absent and at a distance $d_1 + d_2 = 0.14\lambda_0$ from the slits (blue dashed curve).

function of y/λ_0 (solid blue line), where λ_0 is the wavelength associated with the frequency of operation where $\varepsilon_{\text{eff}} \approx \mu_{\text{eff}} \approx -1$. The two slits are clearly discriminated by the lens. When the lens is absent and the total distance between the source plane and image plane is $d_1 + d_2 = 0.14\lambda_0$ (blue dashed curve), the slits can still be distinguished but more imperfectly, despite the greater proximity between the source and the image plane. Indeed, the coupling between the fields radiated by the slits is higher than in the case where the lens is present. The green dashed curve shows the electric field profile at a distance $d_1 + d_2 + L_x = 0.28\lambda_0$ when the lens is absent, and it can be observed that in this scenario it is impossible to discriminate the two slits.

To conclude, we consider the fully 3D scenario wherein both the metamaterial slab and the source are finite along all the

directions of space. To this end, we used an electrically small horizontal dipole antenna with dimensions $L_{dp} = 0.075\lambda_0$ oriented along the z direction. The dipole antenna is located at a distance d_1 above the metamaterial slab with dimensions $L_x = a$, and $L_y = L_z = 30.55a$ [see the inset of Fig. 14(a)]. The microstructure of the metamaterial is the same as in the example of Fig. 13. In Fig. 14(b), we depict (at the plane xoy) the square normalized amplitude of the magnetic field at a distance $d_1 + d_2 + L_x = 0.28\lambda_0$ from the dipole antenna (solid blue curve) in the presence of the lens, and at a distance $d_1 + d_2 = 0.14\lambda_0$ (dashed blue curve) when the lens absent. The HPBW when the lens is present is equal to $0.09\lambda_0$, while when the lens is absent, the HPBW increases to $0.148\lambda_0$. This demonstrates that even in this demanding scenario, the lens still provides a remarkable focusing effect, even more exciting
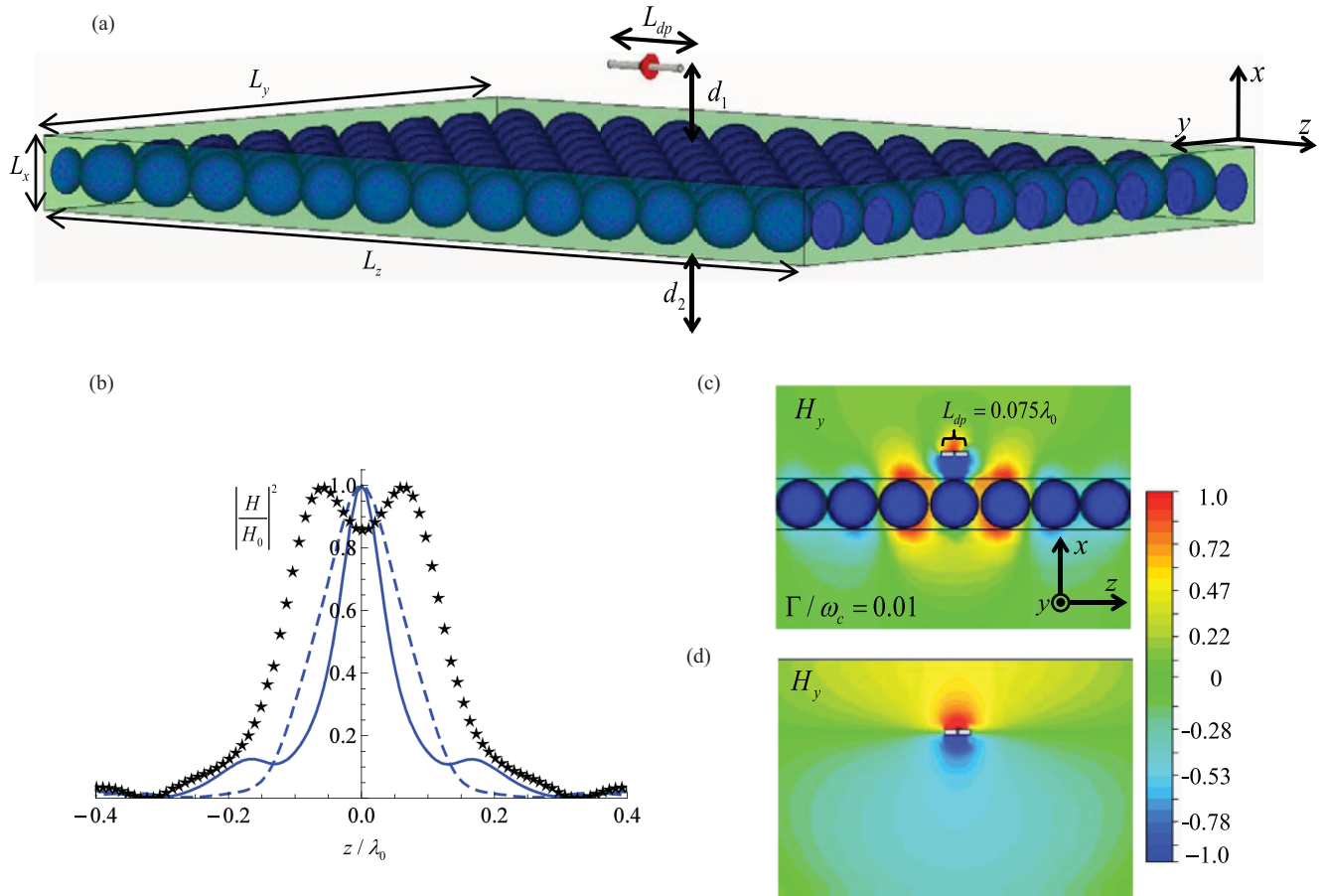
FIG. 14. (Color online) (a) Geometry of the finite-sized plasmonic slab with high-index spherical inclusions. The dipole antenna is located at a distance $d_1 = 0.5L_x$ above the slab with dimensions $L_x = a$, and $L_y = L_z = 30.55a$ (b) Profile of the square normalized magnetic field at a distance $d_2 = 0.5L_x$ below the superlens. (c) Snapshot of the magnetic field radiated by the dipole antenna at the xoy plane. (d) Similar to (c), but in a scenario wherein the lens is absent.

than in the previous cases. However, it must be mentioned that the response of the lens may depend on the specific relative position of the source with respect to the inclusions. In fact, the imaging properties described previously correspond to the case wherein the dipole is placed exactly above a dielectric sphere (center of the unity cell). If the dipole is shifted along the xoy plane into an interstitial place, the magnetic field profile at the image plane is significantly changed [discrete black stars in Fig. 14(b); the HPBW is equal to $0.26\lambda_0$]. Clearly, when placed at an interstitial site the source excites all the neighboring spheres with the same strength, which broadens the beam profile. This happens due to the excitation of higher-order diffraction modes (due to the proximity of the dipole and the metamaterial slab), whose description is beyond the validity of effective medium theory. These results reveal that the granularity of the metamaterial may not be negligible in the near field and show that, when the source is placed in the very near field, the metamaterial cannot be regarded as a truly continuous medium.

Figure 14(c) shows a snapshot in time of the magnetic field at the xoy plane and when the lens is present, whereas Fig. 14(d) shows a similar plot but for the case where the lens is absent. These results suggest interesting applications for metamaterials formed by a plasmonic host and high-index

inclusions in imaging. However, in practice, the realization of such systems with passive natural materials may be difficult. Indeed, it can be checked (not shown here) that the loss of the metamaterial formed by HgTe and TiO_2 considered in Sec. IV is slightly too large to enable a superlensing effect, even though it may permit focusing (based uniquely on the negative index of refraction) limited by diffraction.

VI. CONCLUSION

In this paper, it was shown that metamaterials formed by spherical or cylindrical dielectric inclusions embedded in a plasmonic host medium may imitate an ideal continuous DNG material in a frequency window notably wider than in conventional designs where the role of the inclusions and the host is interchanged. We demonstrated using full-wave simulations that the proposed configurations are less affected by loss than conventional designs and may mimic to some extent the Veselago–Pendry's superlens, enabling a strong broadband negative refraction effect and superlensing. Moreover, due to the long wavelengths of the plasmonic host, the metamaterial response is largely insensitive to disorder. Thus, we believe that the proposed design may be an exciting route to obtain a DNG response in different frequency regimes.

---

*mgoncalo@co.it.pt

[1] V. G. Veselago, Sov. Phys. Usp. **10**, 509 (1968).

[2] J. B. Pendry, Phys. Rev. Lett. **85**, 3966 (2000).

[3] N. Garcia and M. Nieto-Vesperinas, Phys. Rev. Lett. **88**, 207403 (2002).

[4] D. R. Smith, W. J. Padilla, D. C. Vier, S. C. Nemat-Nasser, and S. Schultz, Phys. Rev. Lett. **82**, 1506 (2003).

[5] V. A. Podolskiy and E. E. Narimanov, Opt. Lett. **30**, 75 (2005).

[6] G. Shvets and Y. A. Urzhumov, Phys. Rev. Lett. **93**, 243902 (2004).

[7] A. Alù, A. Salandrino, and N. Engheta, Opt. Express **14**, 1557 (2006).

[8] A. Alù and N. Engheta, Phys. Rev. B **75**, 024304 (2007).

[9] C. Simovski and S. A. Tretyakov, Phys. Rev. B **79**, 045111 (2009).

[10] D. R. Fredkin and I. D. Mayergoyz, Phys. Rev. Lett. **91**, 253902 (2003).

[11] J. T. Costa, M. G. Silveirinha, and S. I. Maslovski, Phys. Rev. B **80**, 235124 (2009).

[12] M. G. Silveirinha, Phys. Rev. B **75**, 115104 (2007).

[13] F. Falcone, T. Lopetegi, M. A. G. Laso, J. D. Baena, J. Bonache, M. Beruete, R. Marqués, F. Martín, and M. Sorolla, Phys. Rev. Lett. **93**, 197401 (2004).

[14] M. G. Silveirinha and N. Engheta, Phys. Rev. B **75**, 075119 (2007).

[15] M. Silveirinha and N. Engheta, Phys. Rev. Lett. **97**, 157403 (2006).

[16] L. D. Landau, E. Lifshitz, and L. Pitaevskii, *Electrodynamics of Continuous Media*, 2nd ed. (Elsevier Butterworth-Heinemann, Oxford, 2004).

[17] J. D. Jackson, *Classical Electrodynamics* (Wiley, New York, 1998).

[18] J. D. Joannopoulos, S. G. Johnson, J. N. Winn, and R. D. Meade, *Photonic Crystals: Molding the Flow of Light*, 2nd ed. (Princeton University Press, Princeton, NJ, 2008).

[19] A.R. McGurn and A. A. Maradudin, Phys. Rev. B **48**, 17576 (1993).

[20] V. Kuzmiak, A. A. Maradudin, and F. Pincemin, Phys. Rev. B **50**, 16835 (1994).

[21] V. Kuzmiak and A. A. Marudin, Phys. Rev. B **55**, 7427 (1997).

[22] A. Raman and S. Fan, Phys. Rev. Lett. **104**, 087401 (2010).

[23] C. L. Holloway, E. F. Kuester, J. Baker-Jarvis, and P. Kabos, IEEE Trans. Antennas Propag. **51**, 2596 (2003).

[24] M. G. Silveirinha, Phys. Rev. B **83**, 165104 (2011).

[25] L. Lewin, Proc. Inst. Elec. Eng. **94**, 65 (1947).

[26] W. G. Spitzer, D. Kleinman, and D. Walsh, Phys. Rev. **113**, 127 (1959).

[27] M. Choi, S. H. Lee, Y. Kim, S. B. Kang, J. Shin, M. H. Kwak, K. Y. Kang, Y. H. Lee, N. Park, and B. Min, Nature **470**, 369 (2011).

[28] N. Matsumoto, T. Hosokura, K. Kageyama, H. Tagaki, Y. Sakabe, and M. Hangyo, Jpn. J. Appl. Phys. **47**, 7725 (2008).

[29] H. C. Guo, W. M. Liu, and S. H. Tang, J. Appl. Phys. **102**, 033105 (2007).

[30] T. Okada, M. Nagai, and K. Tanaka, Opt. Express **16**, 5633 (2008).

[31] J. G. Rivas, C. Janke, P. Bolivar, and H. Kurz, Opt. Express **13**, 847 (2005).

[32] A. Rogalski, Rep. Prog. Phys. **68**, 2267 (2005).

[33] *Landolt-Börnstein—Group III Condensed Matter Numerical Data and Functional Relationships in Science and Technology—New Series*, Subvolume 41B: II-VI and I-VII Compounds; Semimagnetic Compounds, edited by O. Madelung, U. Rössler, and M. Schulz (Springer, Berlin-Heidelberg, 1999).

[34] R. R. Galazka, Phys. Lett. A **32**, 101 (1970).

[35] J. J. Dubowski, T. Dietl, W. Szymanska, and R. R. Galazka, J. Phys. Chem. Solids **42**, 351 (1981).

[36] D. R. Smith, W. J. Padilla, D. C. Vier, S. C. Nemat-Nasser, and S. Schultz, Phys. Rev. Lett. **84**, 18 (2000).

[37] J. Valentine, S. Zhang, T. Zentgraf, E. Ulin-Avila, D. A. Genov, G. Bartal, and X. Zhang, Nature (London) **455**, 376 (2008).

[38] S. F. Rudolph and A. Grbic, IEEE Trans. Antennas Propag. **58**, 1144 (2010); J. Appl. Phys. **102**, 013904, (2007).

[39] CST Microwave Studio Suite 2010 [http://www.cst.com]. The results reported in Figs. 8, 9, 10, 12, 13, and 14 were obtained using open boundaries and the Time Domain (TD) solver of Microwave Studio, whereas the result shown in Fig. 11 was obtained using periodic boundaries and the Frequency Domain (FD) solver of Microwave Studio.

[40] V. C. Nguyen, L. Chen, and K. Halterman, Phys. Rev. Lett. **105**, 233908 (2010).

[41] Y. Xu and H. Chena, Appl. Phys. Lett. **98**, 113501 (2011).

[42] See Supplemental Material at http://link.aps.org/supplemental/10.1103/PhysRevB.84.155131 for the time animation of Fig. 9(b).

[43] See Supplemental Material at http://link.aps.org/supplemental/10.1103/PhysRevB.84.155131 for the time animation of Fig. 10(a).

[44] See Supplemental Material at http://link.aps.org/supplemental/10.1103/PhysRevB.84.155131 for the time animation of Fig. 10(b).

[45] N. Fang, H. Lee, C. Sun, and X. Zhang, Science **308**, 534 (2005).

[46] T. Taubner, D. Korobkin, Y. Urzhumov, G. Shvets, and R. Hillenbrand, Science **313**, 1595 (2006).

[47] M. J. Freire, R. Marques, and L. Jelinek, Appl. Phys. Lett. **93**, 231108 (2008).

[48] S. C. Kehr, Y. M. Liu, L. W. Martin, P. Yu, M. Gajek, S. Y. Yang, C. H. Yang, M. T. Wenzel, R. Jacob, H. G. von Ribbeck, M. Helm, X. Zhang, L. M. Eng, and R. Ramesh, Nat. Commun. **2**, 249 (2011).

[49] The magnetic line source is created in CST Microwave Studio using a waveguide port with a small electric size ($\lambda_0/10$) along the y direction and considering perfect magnetic conductor (PMC) boundary conditions at the $z = $ const. planes.

[50] The electric line source was created in CST Microwave Studio using a waveguide port with a small electric size ($\lambda_0/10$) along the y direction and considering perfect electric conductor (PEC) boundary conditions at the $z = $ const. planes.